Real-Time Simulation of Ultrasound Image Deformation Using Thin Plate Spline

Kian Zalzalah, Sathiyamoorthy Selladurai, and Carlos Rossa
Department of Systems and Computer Engineering
Carleton University, Ottawa, ON, Canada
kianzalzalah@cmail.carleton.ca; SelladuraiSathiyamoo@cunet.carleton.ca; rossa@sce.carleton.ca

***Abstract*—Finite element modelling (FEM) has been the primary approach for non-rigid medical image registration and simulating image deformation in virtual models. A notable limitation of FEM is the high computational cost and the challenges associated with model identification in heterogeneous tissue. In this paper, we propose using thin plate spline (TPS) as an alternative for simulating image deformation during ultrasound-guided needle insertion. Unlike FEM, in TPS non-rigid deformations are simulated by moving a point in the mesh to a target location, and recalculating the location of all other points such that bending energy is minimized, potentially making experimental model identification easier.**

We propose a novel formulation to convert needle-tissue interaction forces, including tissue cutting, friction, and relaxation, into localized nodal displacements that serve as inputs to the TPS model. As the needle moves, it alters the input to the TPS based on its speed, direction, and depth, resulting in a real-time update of the mesh. These updates enable the TPS to adapt continuously, ensuring that the mesh mimics the tissue response. The proposed model is compared against an equivalent FEM model in a series of simulations and experiments in *ex-vivo* porcine tissue. The results show that both models have similar accuracy with TPS being consistently faster than FEM, with improvements in computational efficiency of above 50%. These results confirm the potential of the proposed method to be integrated into ultrasound-guided surgical simulation to enhance precision with larger meshes while reducing computational burden.

I. Introduction

In ultrasound-guided percutaneous surgery (usPS), thin instruments are guided to a target in the tissue through small skin punctures. The procedure is commonly performed under ultrasound image guidance with applications spanning biopsy, brachytherapy, nephrolithotomy, and tumour ablation. While usPS has many advantages over other types of interventions, practitioners often face a steep learning curve and require specialized training to achieve surgical proficiency. This is often attributed to the high level of coordination and dexterity needed to image the tool while steering it towards a target.

The interventionist visualizes the tool with longitudinal or transverse imaging. In longitudinal imaging, they insert the tool so that its shaft travels parallel to the imaging plane, appearing as a line in the 2D image. In transverse imaging, the tool shaft crosses the imaging plane orthogonally, appearing as a bright spot in the image. To maintain visualization and guide the tool tip toward the target, the interventionist must continuously sweep the probe back and forth. Coordinating the hand holding the probe and the hand holding the tool is challenging. In addition, the tool deforms the tissue and pushes the target away from its original location, while also shifting anatomical structures in the ultrasound images [1]. Other challenges, including limitations in image quality and poorly resolved targets, further complicate the procedure, adding to the learning curve and making the procedure outcomes highly operator dependent [2], [3]. In nephrolithotomy, for example, the learning curve only plateaus after 60 interventions and surgical excellence requires 115 trials [4].

To overcome this learning curve, usPS can strongly benefit from surgical simulation. Indeed, physical, virtual, or cyber-physical simulators are nowadays a fundamental component of contemporary surgical training programs, allowing interventionists to practice and hone their skills in a risk-free environment [5]. Such simulators require dynamic, real-time modelling of the tool (like a needle) and tissue interaction to update the simulated ultrasound images in real-time [6]. In usPS, tissue and image deformation models can teach the interventionist how to minimize tissue damage, interpret ultrasound images, and ensure accurate tissue targeting [7].

Traditionally, the biomechanical response of soft tissue to external forces, such as those caused by needle insertion, has primarily been simulated using finite element modelling (FEM). It relies on solving complex partial differential equations describing tissue deformation. FEM has been extensively used to simulate needle insertion, including for needle guidance and tissue trauma assessment in the liver [8], [9], needle steering in brachytherapy [10], [11], [6], and general 2D and 3D image deformation [12], [13]. While accurate, FEM models are computationally expensive and often require specialized hardware, limiting their applicability in portable and small simulators [14], [15]. Furthermore, FEM models often struggle with non-linear tissue response, particularly with large deformations common in needle insertion procedures [11]. Despite advancements in computer power and the development of optimized solvers, the use of real-time FEM simulation in a clinical setting and surgical simulators remains limited [16], [17].

An alternative approach to simulate tissue displacement and the corresponding deformation of ultrasound images is thin plate spline (TPS). TPS was originally developed for interpolating smooth surfaces through a set of control points. Unlike FEM, TPS does not rely on complex partial differential equations but on radial basis functions to interpolate defor-

mations between a set of source and target points, reducing computational complexity making it well-suited for portable applications in surgical simulators [18]. TPS models the image as a mesh of points in space connected by elastic elements. It simulates non-rigid deformations by moving a point in the mesh to a target location, and recalculating the location of all other points such that bending energy is minimized. TPS is used predominantly for image registration. In [19], for example, TPS is used to register ultrasound elastography images of breast tissue with corresponding histopathology images. Similarly, TPS has been applied in 3D ultrasound image registration to account for deformation between adjacent frames. For a comprehensive review on TPS for image registration, please refer to [20], [19], [21]

Since TPS inherently supports non-rigid deformations, it can be effective for simulating the behaviour of soft tissue subjected to cutting and friction during needle insertion and steering. Yet, to the best of our knowledge, TPS has not been used for this purpose. In this paper we propose TPS as alternative to FEM to simulate real-time ultrasound images deformation during usPS. We present a new formulation that models tissue cutting at the needle tip and friction along the needle shaft as localized mesh displacements, which serve as the input to the model. TPS is then used to displace all remaining mesh points accordingly, thereby simulating the resulting tissue deformation and dynamically updating the control points. We show that the proposed method outperforms an equivalent FEM model in terms of computational time by 51.8% while achieving equivalent simulation accuracy.

The paper is structured as follows: Section II introduces the mathematical formulation of TPS. This is followed in Section III by a detailed description of the novel framework proposed to model the interaction between the needle and the tissue as localized mesh point displacements, including friction, tissue cutting, and tissue relaxation. Section IV gives a brief overview of an equivalent FEM model used for comparison purposes. The proposed method is validated experimentally and compared against the FEM model in Section V in terms of computational efficiency and image deformation accuracy. The results are followed by a discussion and the paper concludes with outlines of future work.

II. Thin Plate Spline Based Ultrasound Image Deformation

In the proposed TPS formulation, the tissue is represented as a rectangular mesh of n discrete points $\boldsymbol{\zeta}_s(x, y)$, where x and y give the coordinates of the point within the mesh. These mesh points are evenly spaced by a unit distance k. For example, a point one unit in the positive x-direction from the origin has coordinates $\boldsymbol{\zeta}_s(k, 0)$.

Consider a second mesh where a point is displaced from its original position $\boldsymbol{\zeta}_s(x, y) \in \mathbb{R}^{2\times 1}$ to a new coordinate $\boldsymbol{\zeta}_t(x, y)$. The goal of the TPS to find a transformation $g(x, y) \in \mathbb{R}^2$ to deform the original mesh such that a point $\boldsymbol{\zeta}_s(x, y)$, hereafter referred to as a source point, moves to coordinate $\boldsymbol{\zeta}_t(x, y)$, hereafter referred to as a target point. This

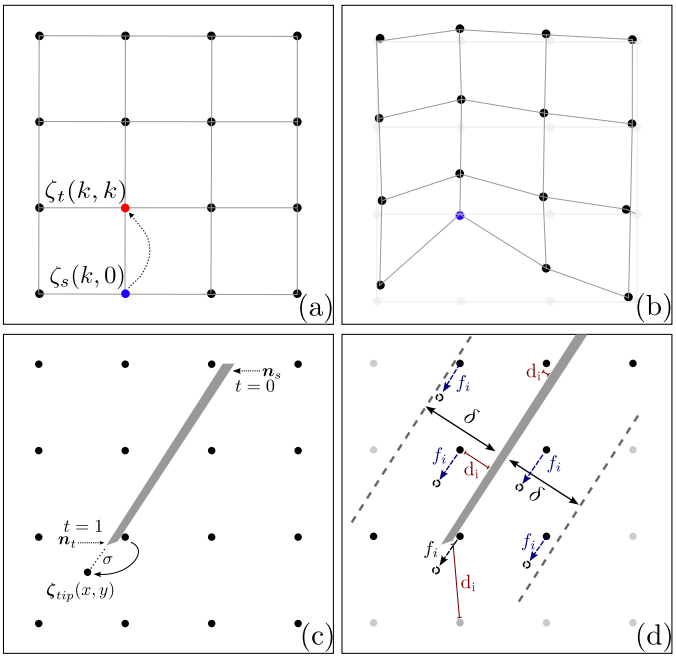

Fig. 1. a) Mesh of points describing source points mapped to a target points. b) Resulting deformation of the mesh. c) Friction threshold in mesh. d) Displacement field due to needle/tissue interaction.

can be illustrated in Fig. 1 (a) and (b) as the source point at $\boldsymbol{\zeta}_s(k, 0)$ is mapped to the target point $\boldsymbol{\zeta}_t(k, k)$. The transformation does so by minimizing an energy function, resulting in smooth deformations of the mesh. The function must be a continuous second-order partial differential equation, such as:

$$\int\int_{\mathbb{R}^2} \left[\left(\frac{\partial^2 g}{\partial x^2}\right)^2 + 2\left(\frac{\partial^2 g}{\partial x \partial y}\right)^2 + \left(\frac{\partial^2 g}{\partial y^2}\right)^2 \right] dxdy \quad (1)$$

The input to the transformation $g(x, y)$ is the coordinate of the i^{th} source point $\boldsymbol{\zeta}_{s_i}(x, y)$ in the original mesh, and the output is the corresponding location of that point in the deformed mesh $\boldsymbol{\zeta}'_{s_i}(x, y)$. The transformation can further be written by a sum of functions that only depend on one component of $g(x, y)$, combining an affine transformation that accounts for global shifts and rotations, and a non-linear deformation governed by a radial basis function, that is

$$g(x, y) = a_0 + a_1 x + a_2 y + \sum_{i=1}^{n\times m} w_i U(r_{ij}). \quad (2)$$

In the above, the coefficients a_0 to $a_2 \in \mathbb{R}^2$ are affine parameters, while w_i is a weight assigned to each of the n source points, determining the influence each source point on the overall deformation of the mesh, and $U(r_{ij})$ is a the radial basis function:

$$U(r_{ij}) = r_{ij}^2 \ln(r_{ij}^2) \quad (3)$$

where $r_{ij} = \|\zeta_{s_i} - \zeta_{s_j}\|$ is the Euclidean distance between the current input to $U(r_{ij})$, i.e., $\boldsymbol{\zeta}_{s_i}(x, y)$, to all other points in the source mesh $\boldsymbol{\zeta}_{s_j}(x, y)$, with $j = 1, 2 \ldots n$.

A symmetric kernel matrix $\mathbf{K} \in \mathbb{R}^{n\times n}$ can now be constructed to gather the distances between all source points, quantifying the relative amount of distortion required to match landmark pairs in the source mesh as

$$\mathbf{K} = \begin{bmatrix} 0 & U(r_{12}) & \cdots & U(r_{1n}) \\ U(r_{21}) & 0 & \cdots & U(r_{2n}) \\ \vdots & \vdots & \ddots & \vdots \\ U(r_{n1}) & U(r_{n2}) & \cdots & 0 \end{bmatrix} \tag{4}$$

Additionally, a matrix of source points $\mathbf{R} \in \mathbb{R}^{n\times 3}$ can be constructed by concatenating all source points with a column of ones to account for global shifts and rotations in the transformation. This allows the model to handle both local deformations and overall linear transformations in the mesh. The matrix of source points is:

$$\mathbf{R} = \begin{bmatrix} 1 & 1 & \dots & 1 \\ \zeta_{s_1} & \zeta_{s_2} & \dots & \zeta_{s_n} \end{bmatrix}^T \tag{5}$$

To calculate the affine parameters a_0 to a_2, and the weighting coefficient w_i of source point i, a matrix $\mathbf{L} \in \mathbb{R}^{n+3\times n+3}$ is constructed from the kernel matrix $\mathbf{K}$ and $\mathbf{R}$ as

$$\mathbf{L} = \begin{bmatrix} \mathbf{K} & \mathbf{R} \\ \mathbf{R^T} & \mathbf{O_1} \end{bmatrix} \tag{6}$$

where $\mathbf{O_1} \in \mathbb{R}^{3\times 3}$ is a matrix of zeros to ensure $\mathbf{L}$ is square. The weights w_i and affine parameters a are:

$$\begin{bmatrix} w_1 & \dots & w_n & a_0 & a_1 & a_2 \end{bmatrix}^T = \mathbf{L}^{-1}\mathbf{V} \tag{7}$$

where $\mathbf{V} \in \mathbb{R}^{n\times 2}$ is a matrix containing all m target points:

$$\mathbf{V} = \begin{bmatrix} \zeta_{t_1} & \zeta_{t_2} & \dots & \zeta_{t_m} & \mathbf{O_2} \end{bmatrix}^T \tag{8}$$

and $\mathbf{O_2} \in \mathbb{R}^{n-m\times 2}$ is a matrix of zeros to give $\mathbf{V}$ the same number of rows as $\mathbf{L^{-1}}$. The new positions $\boldsymbol{\zeta}'_{si}(x, y)$ are computed by using the results of (7) in the initial formulation in (2), resulting in:

$$\zeta'_{s_i} = a_0 + a_1 x + a_2 y + \sum_{i=1}^{n} w_i \|\zeta_{s_i} - \zeta_{s_j}\|^2 \log \|\zeta_{s_i} - \zeta_{s_j}\|^2 \tag{9}$$

Algorithm 1 describes the implementation of the TPS. By solving the inverse problem above, the energy required to deform the source mesh to match the target points is minimized. With the TPS algorithm defined, the goal is to determine a set of target points required to capture tissue deformation during needle-tissue interaction.

Algorithm 1 TPS Calculation

Initialize source points $\boldsymbol{\zeta}_s(x, y)$ and target points $\boldsymbol{\zeta}_t(x, y)$
Compute kernel matrix $\mathbf{K}$ using (4)
Construct system matrix $\mathbf{L}$ using (6)
Compute inverse $\mathbf{L^{-1}}$
Compute TPS affine parameters and weights with (7)
Apply TPS to deform mesh
Update source points $\boldsymbol{\zeta}'_s(x, y)$ using (9)

III. Needle and Mesh Interaction

The goal of the model is to simulate the deformation of the mesh (i.e., the tissue) when a rigid needle is inserted into it. To do so, we create a set of target points connected to the needle shaft. The needle tip enters the mesh at a fixed point $\mathbf{n}_s$ and travels to a position $\mathbf{n}_t$, as shown in Fig. 1. The needle's shaft can be modelled as a straight line from the entry point $\mathbf{n}_s$ to current position of the needle tip $\mathbf{n}_t$, that is:

$$\mathbf{n}(t) = \mathbf{n}_s + t(\mathbf{n}_t - \mathbf{n}_s) \tag{10}$$

where $0 \leq t \leq 1$ is a scalar parameter representing the fractional distance of $\mathbf{n}$ along the needle's path:

$$t = \frac{(\mathbf{n}(t) - \mathbf{n}_s) \cdot (\mathbf{n}_t - \mathbf{n}_s)}{\|\mathbf{n}_t - \mathbf{n}_s\|^2} \tag{11}$$

The interaction between the needle shaft and the tissue can be divided into three main effects: tissue displacement due to tissue cutting at the needle tip, tissue displacement due to friction along the needle shaft, and tissue relaxation.

A. Tissue Deformation at the Needle Tip

At the needle tip, where $t = 1$, the needle pushes the tissue and displaces mesh points further along its insertion direction. We define a target point ahead of the needle tip as:

$$\boldsymbol{\zeta}_{tip} = \mathbf{n}_t + \sigma \cdot \left(\frac{\mathbf{n}_t - \mathbf{n}_s}{\|\mathbf{n}_t - \mathbf{n}_s\|} \right) \tag{12}$$

where σ is the distance of the target point ahead of the needle tip measured along the direction of the needle shaft, as shown in Fig 1(c). This point $\boldsymbol{\zeta}_{tip}$ is the target point for the mesh point that is the closest to the needle tip. In other words, the closest mesh point to the needle tip is deformed to $\boldsymbol{\zeta}_{tip}$ and the neighbouring points are deformed accordingly, thereby capturing how the needle tip pushes the tissue ahead of it.

B. Tissue Displacement due to Friction Along Needle Shaft

Points in the mesh near the needle shaft are affected by friction. Let d_i be the shortest distance between mesh point $\boldsymbol{\zeta}_{s_i}(x, y)$ to the needle shaft, that is:

$$d_i = \min \|\boldsymbol{\zeta}_{si}(x, y) - \mathbf{n}(t)\|, \ \forall\ 0 \leq t \leq 1 \tag{13}$$

We assume that friction affects all the mesh points having a distance $d_i \leq \delta$, where δ is a tunable threshold parameter. Fig. 1(d) shows the distance threshold δ between points that fit the criteria to be affected by friction. We can now define a target point for every mesh point $\boldsymbol{\zeta}_{s_i}(x, y)$ affected by friction as:

$$\boldsymbol{\zeta}_{ti} = \boldsymbol{\zeta}_{si} + f_i \left(\frac{\mathbf{n}_t - \mathbf{n}_s}{\|\mathbf{n}_t - \mathbf{n}_s\|} \right) \tag{14}$$

The above formulation implies that if $\boldsymbol{\zeta}_{s_i}$ is within the threshold, the mesh point moves to target point $\boldsymbol{\zeta}_{t_i}$ which corresponds to the position of the mesh point shifted by f_i units, parallel to the needle shaft. The term in parentheses is the unit vector along the direction of the needle shaft. The mesh displacement f_i due to friction is:

$$f_i = \left(\alpha_1 + \alpha_2 \frac{1}{1 + e^{d_i}} \right) v \tag{15}$$

where v is the needle insertion speed along $\mathbf{n}_t - \mathbf{n}_s$, α_1 is a tunable constant relating the displacement of the source point to the speed, and constant α_2 can be used in the Sigmoid function to so that points farther from the needle are less affected by friction.

C. Tissue Relaxation

Once a mesh point $\boldsymbol{\zeta}_{s_i}$ is moved to $\boldsymbol{\zeta}_{t_i}$ due to friction and the needle stops, the deformed points naturally attempt to return to their original positions over time. This behaviour can be modelled by introducing a relaxation factor α_3:

$$\boldsymbol{\zeta}_{ti} = \boldsymbol{\zeta}_{r_i} + \left(\boldsymbol{\zeta}_{s_i} - \boldsymbol{\zeta}_{r_i}\right) e^{-\alpha_3 t} \tag{16}$$

where $\boldsymbol{\zeta}_{r_i}$ is the position of mesh points before they were displaced by friction, i.e., before (14) is applied. The exponential component above decreases over time, gradually moving the mesh points back toward their original positions. A large α_3 leads to fast relaxation. The exponential decay ensures that the mesh points gradually approach their original positions but never instantaneously, simulating the natural elasticity. Adding tissue relaxation into TPS results in the following modified equation for the deformed mesh points:

$$g(x,y) = a_0 + a_1 x + a_2 y + \sum_{i=1}^{n\times m} w_i U(r_{ij}) + \left(\boldsymbol{\zeta}_s - \boldsymbol{\zeta}_s'\right) e^{-\alpha_3 t}. \tag{17}$$

The needle/mesh interactions determine the positions of landmark points $\boldsymbol{\zeta}_s(x,y)$ and corresponding target points $\boldsymbol{\zeta}_t(x,y)$, see Algorithm 2. As the needle moves, it alters the input to the TPS based on its speed, direction, and depth, resulting in a real-time update of the mesh. These updates enable the TPS to adapt continuously, ensuring that the mesh deforms accurately, mimicking the tissue response.

Algorithm 2 Needle-Tissue Interaction

```
Initialize mesh ζ_s and landmarks.
while needle is moving do
    Update needle tip n_t and compute speed v
    for each mesh point ζ_{s_i} do
        Compute distance: d_i using (13)
        if d_i ≤ δ then
            Compute friction displacement using (14)
        end if
    end for
    Set needle tip target using (12)
    Update mesh using TPS transformation.
    Apply relaxation using (16)
end while
```

IV. FEM-Based Ultrasound Image Deformation

In order to compare the proposed TPS algorithm with a standard FEM model, a brief description of how it can be used to model tissue deformation by discretizing it into a mesh of elements and solving the governing equations of elasticity in a weak form is provided below. Similar to the mesh we

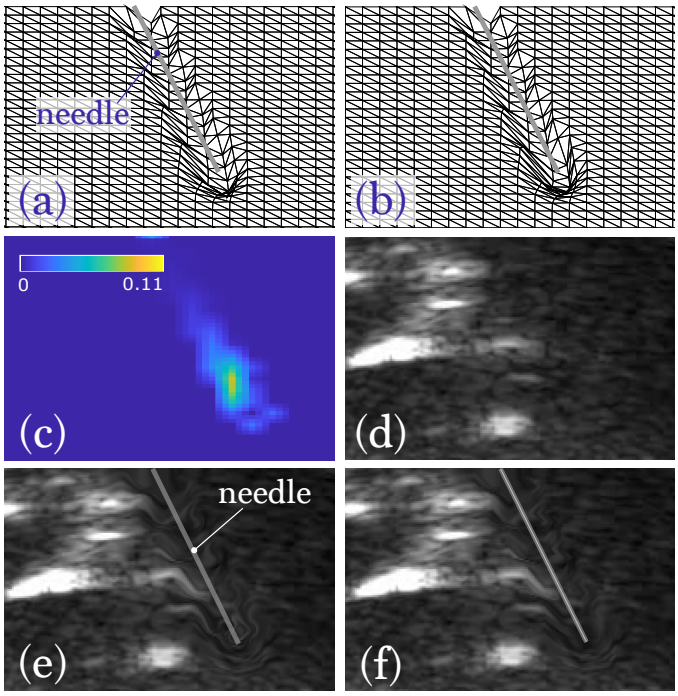

Fig. 2. Simulation results. In (a) and (b) the mesh displacement resulting from needle insertion using TPS and FEM, (c) shows the Cartesian distance ϵ between nodes (a) and (b). When the mesh is applied to the ultrasound image in (d), the resulting images are (e) for TPS and (f) for FEM.

previously described in the TPS algorithm, in FEM the tissue domain $\Omega \subset \mathbb{R}^2$ is modelled by a mesh displacement field

$$\mathbf{u}(x,y) = \begin{pmatrix} u_x(x,y) \\ u_y(x,y) \end{pmatrix}. \tag{18}$$

Under equilibrium, the governing equations are given by $\nabla \cdot \boldsymbol{\mu} = \mathbf{0}$ in Ω where the stress tensor $\boldsymbol{\mu}$ is related to the strain tensor $\boldsymbol{\varepsilon}$ via Hooke's law, i.e., $\boldsymbol{\mu} = \mathbf{C}\,\boldsymbol{\varepsilon}$. For plane-stress conditions, the constitutive matrix $\mathbf{C}$ is

$$\mathbf{C} = \frac{E}{1-\nu^2}\begin{bmatrix} 1 & \nu & 0 \\ \nu & 1 & 0 \\ 0 & 0 & \frac{1-\nu}{2} \end{bmatrix} \tag{19}$$

with E is the tissue's Young's modulus and ν the Poisson's ratio. The strain tensor is expressed as

$$\boldsymbol{\varepsilon} = \begin{bmatrix} \frac{\partial u_x}{\partial x} & \frac{\partial u_y}{\partial y} & \frac{\partial u_x}{\partial y} + \frac{\partial u_y}{\partial x} \end{bmatrix}^T. \tag{20}$$

Multiplying by a test function $\mathbf{v}$ and integrating over the domain yields the weak form:

$$\int_\Omega \boldsymbol{\varepsilon}(\mathbf{v})^T\, \mathbf{C}\, \boldsymbol{\varepsilon}(\mathbf{u})\, d\Omega = \int_{\Gamma_N} \mathbf{v}^T \mathbf{t}\, d\Gamma, \tag{21}$$

where Γ_N is the portion of the boundary with prescribed traction $\mathbf{t}$. Discretizing Ω into finite elements and approximating the displacement field with shape functions $N_i(x,y)$,

$$\mathbf{u}(x,y) \approx \sum_{i=1}^{N} \mathbf{u}_i\, N_i(x,y) \tag{22}$$

leads to the system of linear equations:

$$\mathbf{K}\,\mathbf{u} = \mathbf{F}, \tag{23}$$

where $\mathbf{K}$ is the global stiffness matrix and $\mathbf{F}$ is the load vector, which includes all forces applied to the tissue during needle insertion, including the tissue cutting force at the needle tip, and viscous friction between the needle shaft and the tissue modelled as a distributed load in the mesh [6].

V. Experimental Validation and Results

To validate the proposed algorithms and assess its performance against the equivalent FEM model, a set of simulations and experiments on *ex-vivo* tissue are performed. First, a mesh of 1200 points is created for both TPS and FEM algorithms. In the FEM model, four different tissues types are considered, ranging from soft to stiffer, by setting the Young's modulus E to 10^4, 8^4, 5^4, and 10^3 Pa, with a Poisson's ratio of $\nu = 0.45$, which is within the range of biological tissue [22]. A needle is then inserted at a oblique angle from the top of the mesh with a needle tip cutting force of $F = 0.4$ N, and friction constant of 10^{-5} Ns/m, as per [11]. The mesh displacement is evaluated using the FEM simulation for 50 discreet needle insertion depths. The displacement of every mode in the mesh is then evaluated at depth.

Following the FEM simulation, an equivalent TPS model is run. Since the TPS model parameters cannot be calculated from those of the FEM model, the TPS must be tuned to match the FEM. If $\epsilon = ||\mathbf{g}(x,y) - \mathbf{u}(x,y)||$ is the Cartesian distance between equivalent nodes in the TPS and FEM mesh, the mean absolute error (MAE) and root mean square error (RMSE) between the N nodes with non zero displacement ($\epsilon \neq 0$) is

$$\text{MAE} = \frac{1}{N}\sum_{N}\epsilon, \qquad \text{RMSE} = \sqrt{\frac{1}{N}\sum_{N}\epsilon^2}. \tag{24}$$

To model the parameters that minimize the MAE with respect to the FEM model, the TPS is run 2000 times, each using a different combination of K, α_1, and α_2. A sample result showing the FEM nodal displacement, and that of the TPS with the lowest MAE is shown in Fig. 2(a) and (b). Fig. 2(c) shows the error ϵ between them, indicating that by accurately tuning the TPS model, the error is negligible. Next, each point in the mesh is matched to a pixels in the sample ultrasound image shown in Fig. 2(d) to simulate image deformation caused by needle insertion. The result for TPS and FEM models can be seen in Fig. 2(e) and (f).

MAE and RMSE between the TPS and FEM simulations for nodes with ($\epsilon \neq 0$) are shown in Fig. 3(a). As expected, the error increases as the tissue Young's modulus decreases, yet it remains under 10^{-3} on a 1200 point mesh. Finally, the average simulation time for each of the 50 needle insertion steps in all simulations is computed for both the TPS and FEM models on an intel i5 computer with 16 Gb of RAM. Both simulations are executed in Matlab on a mesh size ranging from 500 to 4500 nodes. The results shown in Fig. 3(b) indicate that the TPS simulation is on average 51.8% faster than the FEM model, while achieving similar mesh displacement outputs.

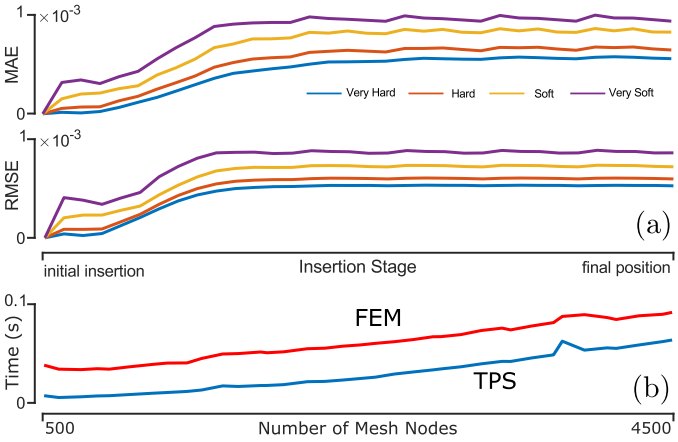

Fig. 3. Mesh displacement error between TPS and FEM for different tissue types (a) and average simulation time as a function of the number of mesh nodes in the simulation (b).

The model performance is further evaluated via a piece of porcine *ex-vivo* tissue following the experiment depicted in Fig. 4. A 18G needle is inserted into the tissue, just under the imaging plane of an ATL C5-2 ultrasound probe placed on the other side of the sample. A region of interest (ROI) of approximately 2x3 mm with 200 pixels is defined and placed at a constant distance ahead of the needle tip. As the needle is manually and slowly pushed into the tissue, the ROI moves towards the probe. Ultrasound images of the ROI taken before the needle is inserted and during needle insertion are then compared using the speckle tracking algorithm described in [23]. Both a FEM and TPS mesh are created with the same number of nodes and resolution as there are pixels in the ultrasound image. The model parameters of both simulations are then optimized separately to minimize the RMSE between the speckle displacement of each pixel in the ROI and each corresponding mesh node displacement for a number of discreet needle insertion steps.

The RMSE between the displacement of all 200 pixels in the ROI in 8 different image frames, and the displacement of the equivalent nodes in the FEM and TPS models is shown in Fig. 5(a). The total axial displacement of the pixels in the 40x40 mm US images at depths 2 and 9 mm are shown in (b) and (c). The RMSE between the two models is statistically the same and the error remains under 0.02 mm, confirming the accuracy of the proposed model in capturing tissue displacement.

VI. Conclusion

FEM has been the primary model used in medical imaging for non-rigid image registration and simulating image deformation in virtual models. In this paper, we propose TPS as an alternative modelling approach to FEM, specifically for ultrasound image deformation induced by a needle inserted in the tissue. We devised a new formulation to convert needle/tissue

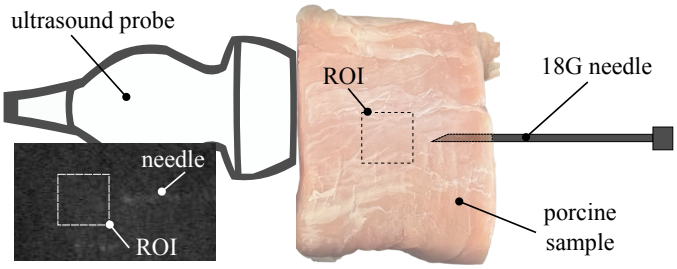

Fig. 4. Experimental setup to evaluate the model performance on the ex-vivo porcine tissue shown in the image. Speckle displacement is tracked within the region of interest (ROI), kept at a constant distance ahead of the needle tip.

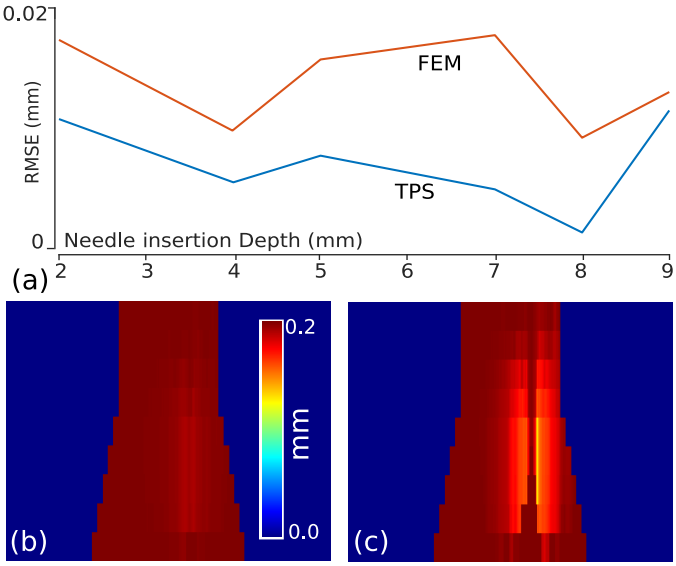

Fig. 5. RMSE between speckle displacement in the ROI and TPS and FEM nodal displacement (a). In (b-c), the measured speckle displacement at depth 2 and 9 mm with the needle inserted from the centre bottom of the image.

interaction forces into suitable mesh displacement inputs to the TPS model. To the best of our knowledge, this modelling approach has not been proposed before. This contribution can make image displacement model identification easier than the traditional FEM models, as the input to the mesh can be obtained from speckle displacement measured experimentally, rather than tissue characterization.

Simulation and experimental results show that the TPS and FEM models can achieve similar accuracy when optimized to match one another. Notably, TPS is consistently faster than FEM, showing improvements in computational efficiency of above 50% on a regular desktop computer. The model was validated experimentally on *ex-vivo* tissue, further confirming the accuracy of the proposed framework. Currently, the mesh is assumed to have an homogeneous and linear stiffness constant. In future work, the model will be extended to account for nonlinearity and heterogeneity in the tissue. In addition, a more thorough experimental evaluation on different tissue samples should be conducted to further establish model accuracy. Furthermore, future work will develop a speckle model of the needle to be included in the images.

References

[1] H. Mazdarani, A. Cotton, and C. Rossa, "2D ultrasound-guided visual servoing for in-plane needle tracking in robot-assisted percutaneous nephrolithotomy," in *IEEE Inter. Conf. on Systems, Man, and Cybernetics*, 2023, pp. 1786–1791.

[2] F. Ng, K. K. others, and S. K. Lim, "Ultrasound-guided percutaneous nephrolithotomy: Advantages and limitations," *Investigative and Clinical Urology*, vol. 58, no. 5, p. 346, 2017.

[3] M. Trojak *et al.*, "Mixed Reality Biopsy Navigation System Utilizing Markerless Needle Tracking and Imaging Data Superimposition," *Cancers*, vol. 16, no. 10, p. 1894, 2024.

[4] Y. Song *et al.*, "Evaluating the learning curve for percutaneous nephrolithotomy under total ultrasound guidance," *PloS one*, vol. 10, no. 8, p. e0132986, 2015.

[5] A. Lelevé, T. McDaniel, and C. Rossa, "Haptic training simulation," *Frontiers in virtual reality*, vol. 1, p. 3, 2020.

[6] C. Rossa and M. Tavakoli, "Issues in closed-loop needle steering," *Control engineering practice*, vol. 62, pp. 55–69, 2017.

[7] Y. Adagolodjo, L. Goffin, M. de Mathelin, and H. Courtecuisse, "Inverse real-time Finite Element simulation for robotic control of flexible needle insertion in deformable tissues," in *IEEE Inter. Conference on Intelligent Robots and Systems*, 2016, pp. 2717–2722, iSSN: 2153-0866.

[8] H. Mohammadi, A. Ebrahimian, and N. Maftoon, "Finite-Element Modelling of Needle-Tissue Interactions," *Archives of Computational Methods in Engineering*, vol. 31, no. 3, pp. 1363–1404, 2024.

[9] Y. Kobayashi *et al.*, "Development of an integrated needle insertion system with image guidance and deformation simulation," *Computerized Medical Imaging and Graphics*, vol. 34, no. 1, pp. 9–18, 2010.

[10] O. Goksel, K. Sapchuk, and S. E. Salcudean, "Haptic simulator for prostate brachytherapy with simulated needle and probe interaction," *Transactions on haptics*, vol. 4, no. 3, pp. 188–198, 2011.

[11] M. Khadem, C. Rossa, R. Sloboda, N. Usmani, and M. Tavakoli, "Mechanics of Tissue Cutting During Needle Insertion in Tissue," *Robotics and Automation Letters*, vol. 1, no. 2, pp. 800–807, 2016.

[12] B. Burger, S. Bettinghausen, M. Radle, and J. Hesser, "Real-time gpu-based ultrasound simulation using deformable mesh models," *Transactions on medical imaging*, vol. 32, no. 3, pp. 609–618, 2012.

[13] L. Han *et al.*, "Fast deformation simulation of breasts using gpu-based dynamic explicit finite element method," in *Digital Mammography International Workshop*. Springer, 2010, pp. 728–735.

[14] H. Xie, J. Song, Y. Zhong, and C. Gu, "Kalman filter finite element method for real-time soft tissue modeling," *IEEE Access*, vol. 8, pp. 53 471–53 483, 2020.

[15] W. Hou, P. X. Liu, and M. Zheng, "A new model of soft tissue with constraints for interactive surgical simulation," *Computer Methods and Programs in Biomedicine*, vol. 175, pp. 35–43, 2019.

[16] M. Kaya *et al.*, "Visual tracking of multiple moving targets in 2D ultrasound guided robotic percutaneous interventions," in *IEEE Inter. Conference on Robotics and Automation*, 2017, pp. 1996–2002.

[17] S. Frisken *et al.*, "A comparison of thin-plate spline deformation and finite element modeling to compensate for brain shift during tumor resection," *Inter. Journal of Computer Assisted Radiology and Surgery*, vol. 15, no. 1, pp. 75–85, 2020.

[18] C. Rossa, M. Najafi, M. Tavakoli, and K. Adams, "Nonlinear workspace mapping for telerobotic assistance of upper limb in patients with severe movement disorders," in *IEEE Inter. Conference on Systems, Man, and Cybernetics*, 2017, pp. 2255–2260.

[19] B. Chuang *et al.*, "Interpreting ultrasound elastography: Image registration of breast cancer ultrasound elastography to histopathology images," in *IEEE Inter. Symposium on Biomedical Imaging*, 2010, pp. 181–184.

[20] K. Rohr *et al.*, "Landmark-based elastic registration using approximating thin-plate splines," *IEEE Transactions on Medical Imaging*, vol. 20, no. 6, pp. 526–534, 2001.

[21] B. Lin and Y. Sun, "Thin Plate Spline Feature Point Matching for Organ Surfaces in Minimally Invasive Surgery Imaging," vol. 8671, p. 12, 2013.

[22] E. Dehghan *et al.*, "Parameter Identification for a Needle-Tissue Interaction Model," in *2007 29th Annual International Conference of the IEEE Engineering in Medicine and Biology Society*, Aug. 2007, pp. 190–193, iSSN: 1558-4615.

[23] S. Selladurai and A. K. Thittai, "Strategies to obtain subpitch precision in lateral motion estimation in ultrasound elastography," *IEEE Transactions on Ultrasonics, Ferroelectrics, and Frequency Control*, vol. 65, no. 3, pp. 448–456, 2018.